Implosion of D_2 temperature-controlled cryogenic foam targets with plastic ablators

A. Richard,[1,2] K. A. Tanaka,[1,3] K. Nishihara,[1] M. Nakai,[1] M. Katayama,[1] Y. O. Fukuda,[1] T. Kanabe,[1,3] Y. Kitagawa,[1] T. Norimatsu,[1] M. Nakatsuka,[1] T. Yamanaka,[1] M. Kado,[1] T. Kawashima,[1] C. Chen,[1] M. Tsukamoto,[1] and S. Nakai[1,3]

[1]*Institute of Laser Engineering, Osaka University, Suita, Osaka 565, Japan*

[2]*Commissariat à l'Energie Atomique, Centre d'Etudes de Limeil-Valenton, 94195 Villeneuve Saint Georges Cedex, France*

[3]*Department of Electromagnetic Energy Engineering, Osaka University, Suita, Osaka 565, Japan*

(Received 26 July 1993)

The implosion hydrodynamics of temperature-controlled cryogenic deuterium foam targets with plastic ablators is investigated. The experimental data recorded with x-ray imaging systems are compared to a one-dimensional (1D) simulation. The ablation front trajectories derived from x-ray streak-camera data agree with 1D simulation. However, an x-ray core emission is observed at an earlier time, and for a longer duration than that predicted. For the three liquid-fuel shots, the convergence ratios are, respectively, 0.4, 0.9, and 0.7 times that predicted by the 1D simulation.

PACS number(s): 52.40.Nk, 52.70.La, 52.35.Py

I. INTRODUCTION

A density of about 1000 times the DT liquid density and a temperature of about 5 keV at the center of the compressed target are necessary for thermonuclear ignition. Directly driven targets have reached imploded densities of 200 times the liquid density of DT with glass microballoons [1] and of 600 times the liquid density of DT with plastic hollow shell targets [2]. However, the measured neutron yields were typically two to three orders of magnitude less than predicted by the simulation. The observed neutron yields were close to the ones created at the time of shock waves colliding at the target center for the second time in the simulation. The shock waves were released from the imploding shells at early times and propagate ahead of the shells. The significant fuel stagnation and compression occur after this second shock collision at the target center, indicating that the implosions did not result in creating a hot spark which could have produced more neutrons. These discrepancies are most probably explained by the nonuniformity of the implosion and the subsequent development of hydrodynamic instabilities. Thus it is of importance to study the detailed hydrodynamics of the implosion. We will describe in this paper the implosion hydrodynamics of temperature-controlled cryogenic deuterium (D_2) foam targets with plastic ablators using the data recorded with x-ray imaging systems.

II. DESCRIPTION OF THE EXPERIMENT

The GEKKO XII laser facility [3] uses a Nd:glass laser whose wavelength was converted to 0.53 μm for that experiment. It provides 12 beams disposed on a dodecahedral geometry. The laser energy for the presented results was typically 8 kJ. The time profile of the pulses had a flat top of 1-ns duration with a Gaussian rise of 1 ns, with a full width at half maximum (FWHM) of 2.5 ns. The energy imbalance of the 12 beams was better than 5% rms. Random phase plates [4] were used in order to improve the laser irradiation uniformity. The laser was focused with the condition $d/R_0 = -5$, where d is the distance between the focal point and the center of the target and R_0 is the target initial radius.

The targets are based on CH foam hollow shells coated with a CH layer [5]. Plastic is used because its atomic number and mass density are low. The inner foam layer acts as a sustainer of the deuterium fuel when it is liquid or solid. The outer plastic layer works as an ablator intended to reduce the preheat by high-energy electrons and shock waves and also as a shield of the D_2 fuel. The shells were produced using water-oil-water emulsion method [6] and the coating was performed by the interfacial polycondensation method [7]. The cell size of plastic foam is less than 1 μm. The surface roughness of the ablator is estimated to be less than 0.02 μm from electron scanning microscope pictures. The sphericity and the uniformity are better than 98%.

The shells were filled, at the center of the irradiation chamber, with D_2 between 80 and 110 atm at room temperature by diffusion, to saturate the given foam layer at the intended cryogenic temperature [8]. The temperature of the targets was controlled from 12 to 35 K in order to shoot it with the fuel in solid, liquid, or gas phase. The diameter of the shells was varied from 530 to 702 μm and the foam layer from 10 to 12 μm in thickness. The foam density was 0.22 g cm^{-3}. The CH ablator thickness was 4 μm. The CH coating density was about 1.2 g cm^{-3}.

We looked at the time evolution of the implosion process using an x-ray streak camera (XSC) and two x-ray framing cameras (XFC) coupled with pinhole imaging systems. The XSC used a copper iodine (CuI) photocathode and the two XFC's used reflective-type photocathodes of either 1-μm-thick copper iodine (CuI) or 1 μm gold [9]. The combination of photocathodes and Be and Saran filters give the ranges of transmission above 1 keV for the XSC and above 1.4 keV for the XFC's. The spatial and time resolutions were, respectively, 20 μm and

20 ps (with an 80-μm slit) for the XSC. The temporal resolution is 83 ps [10] with a 100-ps frame interval for each XFC and the spatial resolution is 20 μm. The two XFC's are adjusted in timing to observe the entire history of implosions. X-ray pinhole cameras are also used to monitor time-integrated, 1–2-keV x-ray images. A Ag counter and plastic scintillators were used to monitor primary neutrons, while plastic scintillators are used also for measuring the secondary neutrons, due to the reaction of the primary deuterons with the secondary tritons, to estimate the density radius products [11].

III. EXPERIMENTAL AND SIMULATED RESULTS

We would like to concentrate on the liquid-fuel shells for which we have three reproducible data shots. The ablative implosion process of a cryogenic fuel foam shell may be divided into the following phases [12]. The strong shock driven by the laser irradiation propagates through the shell and then into the fuel saturated vapor, until it collapses at the center of the target. The shell starts accelerating after the shock transverses until the speed of the shell reaches a peak speed determined by the force balance between the ablation pressure and the shell mass. The shock is reflected at the center of the target, propagating outward until it collides with the imploding contact surface. The motion of the shell is then slowed down by the pressure of the inner fuel. The shell kinetic energy is transformed into thermal energy. The shell stagnates and the maximum compression is achieved. The inner fuel pressure overcomes the dynamic pressure of the shell, which starts moving outward; thermal energy is reconverted into kinetic energy. During this implosion process neutrons are emitted due to heating by the shock (shock-wave neutrons) and the stagnation phase (compression neutrons). The recorded x-ray emission comes from the conduction region close to the ablation front during the acceleration, inertial, and expansion phases. The x-ray emission comes also from the compressed core and the conduction region during the stagnation phase. Here the conduction region is defined as the one between the cutoff and the ablation layers. The x-ray intensity from the core at its maximum intensity overwhelms the one from the ablation region.

We show in Fig. 1 the pictures recorded with the XSC [Fig. 1(a)], one XFC [Fig. 1(b)], and the pinhole camera [Fig. 1(c)] for a liquid-fuel cryogenic target (shot no. 12865). Laser energy was 7.8 kJ with 4.7% rms beam energy balance. Its diameter was 702 μm, the ablator and the foam thicknesses were 4 and 10 μm. It was filled with 80 atm D_2 and was cooled at 22 K. Detailed conditions for three liquid shots are summarized in Table I. We can see from the XFC that the compression remains nearly spherical with a slight low mode nonuniformity, probably due to the beam imbalance. The trajectory of the implosion by the XSC appears very symmetric, even in the expansion phase. The x-ray pinhole picture shows also a symmetric implosion. Another feature in this time-integrated picture is that a cold, thus less emitting region,

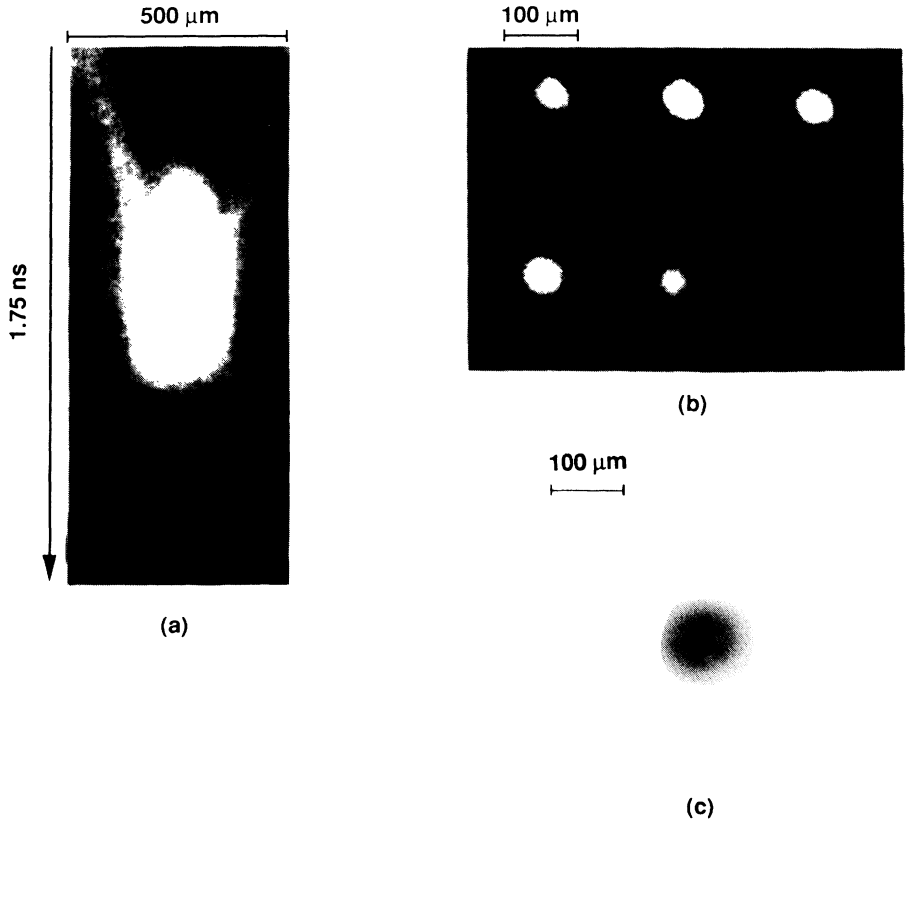

FIG. 1. Records of the x-ray emission for the liquid-fuel shot no. 12865. (a) The XSC imaging system. (b) The second XFC imaging system, around maximum compression. (c) The pinhole imaging system.

TABLE I. Experimental conditions for the three cryogenic deuterium shots at liquid temperatures.

Shot no.	Beam balance %	Energy (kJ)	D_2 pressure (atm)	D_2 temperature (K)	Initial diameter (μm)	Foam thickness (μ m)
12 834	4.0	8.6	100	19.8	595	12
12 847	3.1	7.6	110	26	530	10
12 865	4.7	7.8	80	22	702	10

surrounds the hot strongly emitting region, indicating that most of the shell has stayed spherically stable until the stagnation phase.

On the *r-t* flow diagram given by the one-dimensional (1D) simulation for shot no. 12865 we have plotted (Fig. 2) the location of the ablation front from the XSC data. Without a time fiducial in the experiment we adjusted the XSC data to the 1D simulation. The agreement is very good for the acceleration and the inertial phases, however, the compression appears halted earlier than predicted by the code HISHO. These tendencies are commonly shared among the other shots. From these ablation front trajectories we derived average implosion velocities. We found 1.9×10^7, 1.8×10^7, and 2×10^7 cm s^{-1}, respectively, for shot nos. 12834, 12847, and 12865 (hereafter we give the numerical values in the same shot order). These values are in good agreement with the value of 2×10^7 cm s^{-1} given by the simulation. Both wings of the XSC pictures, which are emitted from the ablation region, allowed us to calculate an average velocity imbalance. These velocity imbalances are of the same order: 5.4%, 6.2%, and 7.5%, to be compared with the values of the beam energy imbalances, respectively, 4%, 3.1%, and 4.7%, also close to each other. Neutron yield was 5×10^7 and $\rho\Delta R_{\text{fuel}}$ was 8 mg/cm^2 for no. 12865 and similar values were observed for the other two shots. The ratio of the observed to the simulated results is 5×10^{-3} for neutrons and 0.3 for $\rho\Delta R$.

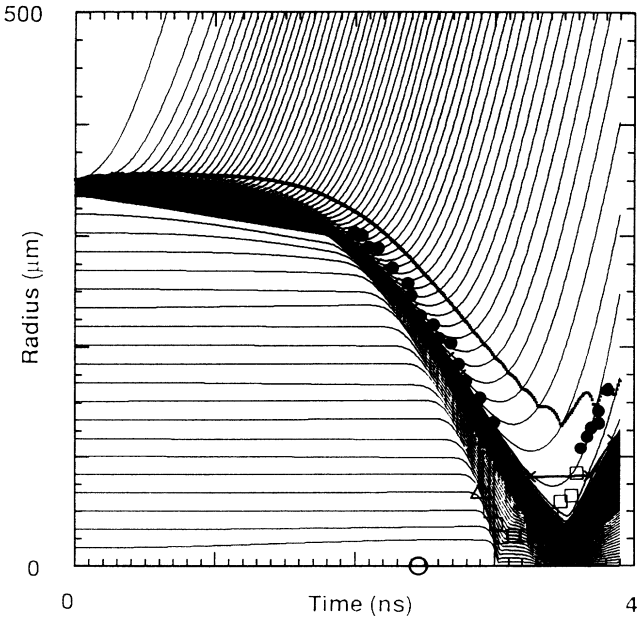

FIG. 2. Data taken from the experimental radial profiles of the x-ray emission recorded by the XSC are plotted on the 1D HISHO radius-time (*r-t*) flow diagram; ●: ablation front; □: the HWHM of the core emission; ○: shock at the center; △: reversed shock at the contact surface for shot no. 12865.

The experimental and simulated time profiles of the compressed core emission are shown in Figs. 3, 4, and 5 for shot nos. 12834, 12847, and 12865, respectively. We remark first that for all the shots the profiles of the experimental cores have a duration longer and start earlier than that predicted by the simulation. The time differences between the simulated and experimental x-ray emission maxima are 150, 190, and 185 ps. The experimental FWHM's of the time profiles of the x-ray emission are 275, 200, and 267 ps; these values have to be compared with the simulated ones: 128, 142, and 153 ps. The difference is least for shot no. 12847. Such an early emission was already observed in previous experiments with foam cryogenic targets without plastic coating [13,14]. It has been confirmed by the simulation that this preemission is not due to the preheat in the shells. In Ref. [15], with an x-ray streak-camera imaging system the stagnation phase lasted also longer than predicted by the simulation. It was explained by the presence of hot and cold regions ($\sim$ 20 μm scale size) in the focal spots of individual beams, from 0.5 to 2 times the nominal intensity. Those were due to both phase errors in the ir laser and the conversion to 0.35 μm. Because of these modulations in intensity the observed trajectory at ablation front is a weighted average between the ones from 0.5 to 2 times the nominal intensity. In our case the laser wavelength was converted to 0.53 μm and random phase plates (RPP's) were used to improve the uniformity of the irradiation, so that the formation of hot and cold spots should be less. The focal spot with RPP's seems rather smooth, though the focal spot envelope consists of many speckle patterns of 5–10 μm spatial scale. These speckle patterns could be smoothed out by the thermal electrons.

Let us describe briefly the simulation code HISHO [16] used for the comparison with the experiment. HISHO is a 1D Lagrangian hydrodynamics code based on a two-temperature (ion and electron) fluid model. It uses the multigroup diffusion model for radiation transport and the average atom local thermodynamic equilibrium (LTE) model to calculate the ionization state and the electron level population. Pressure ionization, Fermi degeneracy, and Coulomb interaction are taken into account for modeling the high-density and cold matter. A value of 0.6 was used for the electron flux limiter. The shape of the laser pulse is based on the measured one, but closely approximated by a sum of Gaussian pulses with a fitting rate of 95%. The preheat by hot electrons is taken

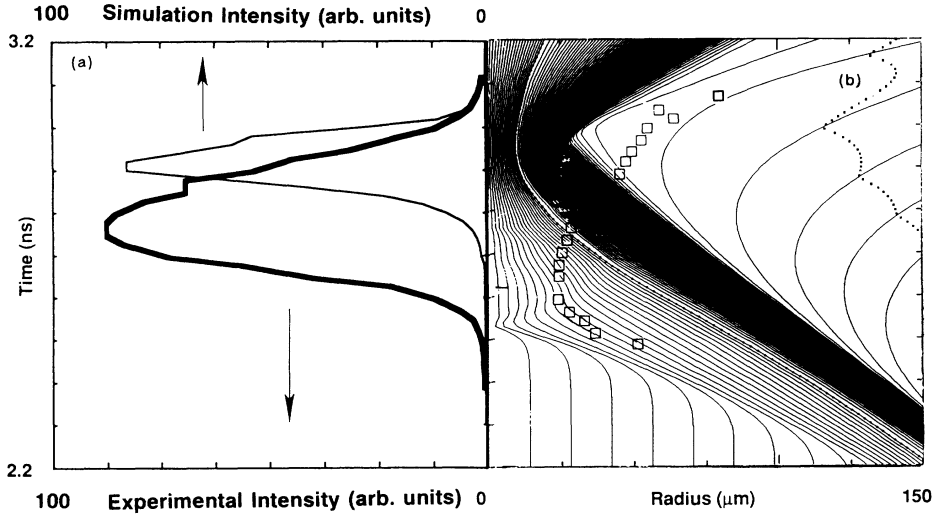

FIG. 3. The x-ray core emission of shot no. 12834. (a) Comparison of the simulated and the experimental (recorded by the XSC) time profiles at center of the target (left). (b) The observed spatial HWHM of the central emission is plotted on the 1D HISHO *r-t* flow diagram (right).

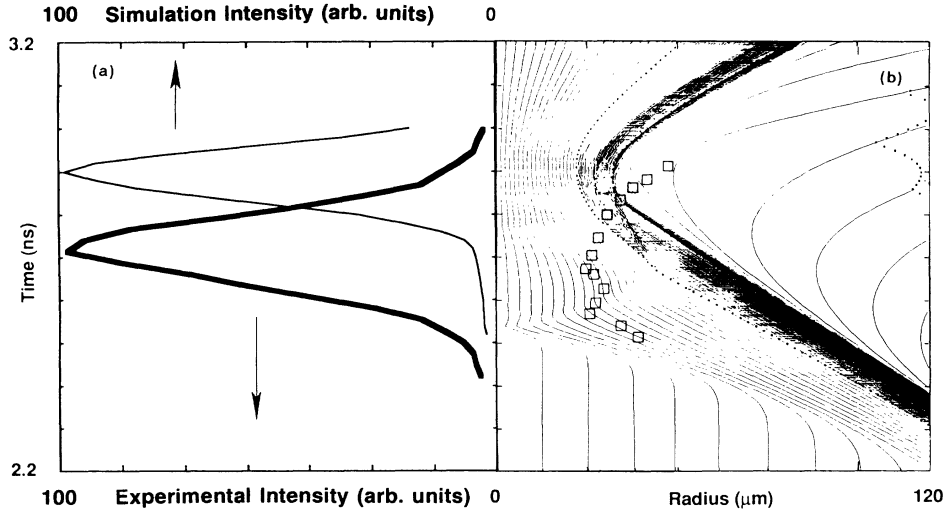

FIG. 4. The x-ray core emission of shot no. 12847. (a) Comparison of the simulated and the experimental (recorded by the XSC) time profiles at the center of the target (left). (b) The observed spatial HWHM of the central emission is plotted on the 1D HISHO *r-t* flow diagram (right).

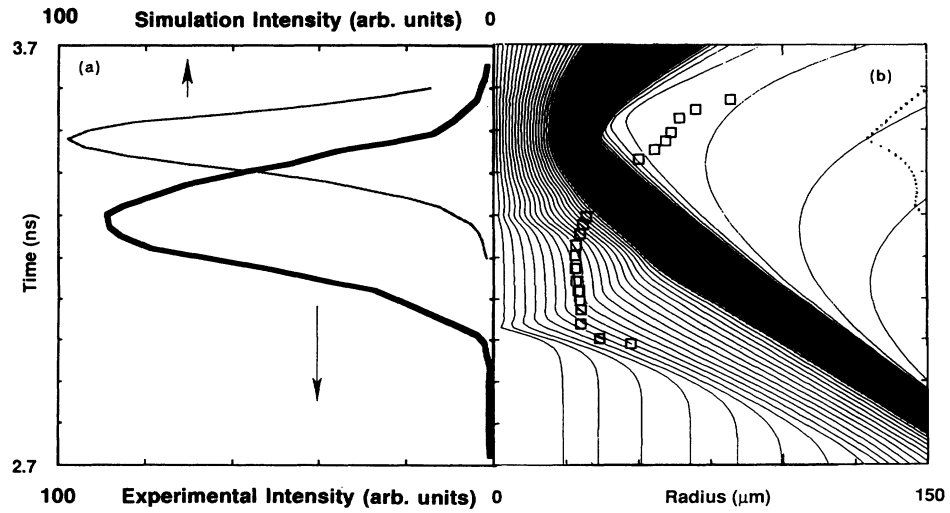

FIG. 5. The x-ray core emission of shot no. 12865. (a) Comparison of the simulated and the experimental (recorded by the XSC) time profiles at the center of the target (left). (b) The observed spatial HWHM of the central emission is plotted on the 1D HISHO *r-t* flow diagram (right).

into account from planar target experiments [17,5]. The CH ablator thickness of 4 μm corresponds to a preheat level of about 20 eV.

IV. DISCUSSION

A. Explanation of the radial profiles of the x-ray emission recorded by the XSC

The x-ray emission observed by the x-ray streak camera is simulated by a ray tracing as a post processor of the 1D HISHO, which uses a radiative-transfer equation. The emission and absorption for free-free, free-bound, and bound-bound transitions are included. This model takes into account the spatial resolution of the x-ray streak-camera imaging system but not its time resolution. In Fig. 6 on the *r-t* flow diagram given by HISHO, we have plotted the following features taken from the simulate radial profiles: (1) The maximum of the x-ray emission from the conduction zone, which gives us the location of the ablation front (shown as multiplication symbols in the figure); (2) the half-width at half maximum (HWHM) of the core emission (shown as open squares); (3) the time of the emission due to the collapse of the shock at the center (shown as open circles); (4) the time of the emission due to the reflected shock hitting the contact surface (shown as open triangles). We define here the shell density interface as the location where the shell density increases suddenly in the radial direction after the reversed shock hits the contact surface (indicated in Fig. 6). From the simulation the first emission comes from the center of the target due to the shock arriving at the center. Then the reversed shock collides with the imploding target shell, appearing as small lateral peaks just inside the ablation peaks. We observe that at around the maximum compression the ablation front location is not representative of the surface of the shell any more. On the contrary, the HWHM of the core emission gives the approximate location of the contact surface between hot, low-density core and cold, high-density foam-fuel layer with a $\sim$5-μm precision. This characteristic is common for all the liquid- and solid-fuel shots. Shown in Fig. 7 are the radial profiles plotted from the measurement [Fig. 7(a)] and calculated by the simulation [Fig. 7(b)], at different times of the implosion process of a liquid-fuel cryogenic foam shell (no. 12865). All of the above simulated features are seen in the measured x-ray signals of Fig. 7(a). In Fig. 7(b) the simulated features in Fig. 6 are displayed also and show similarities with the experiment.

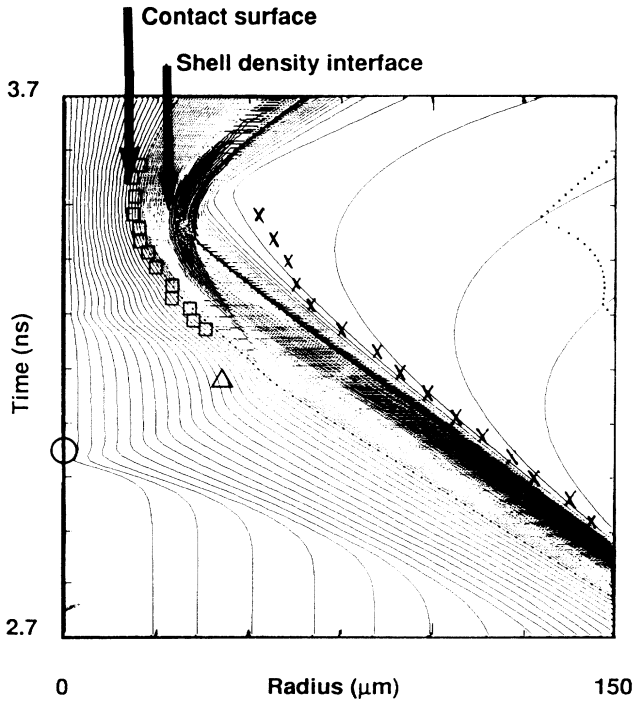

FIG. 6. Shot no. 12865. Data taken from the simulated radial profiles of the x-ray emissions are plotted on the 1D HISHO *r-t* flow diagram. *X*: ablation front; □: the HWHM of the core emission; ○: shock at the center; and △: reversed shock at the contact surface.

Shot no. 12865 presents a small central peak of x-ray emission early in time which may be due to the collapse of the shock at the center [Figs. 2 and 7(a)]. Two small peaks are also observed such as those observed in the simulation when the reflected shock hits the contact surface [Figs. 2 and 7(a)]. The timing of the propagation of the shock, given by these emission, is earlier than predicted by the simulation. For example, the small peaks due to the shock colliding with the imploding shell are observed in the experiment 230 ps earlier than in the simulation (shot no. 12865).

B. Description of the experimental time profiles of the x-ray emission based on the simulation

In the experiment (no. 12834) one can see two temporally separated peaks and shoulders in Fig. 3, though the timing is 150 ps different from the prediction. The simulated time profile in Fig. 3 indicates that two major peaks of x-ray core emission can occur. The first one corresponds to the time when the shell density interface reaches the best convergence. The second peak is due to the maximum compression of the shell surface. The shell itself is recompressed by the expansion of the shell density interface. The first and second peaks show time lag of about 50 ps for shot no. 12834, while the first and second occurred at almost the same timing for no. 12847 (Fig. 4) and 12865 (Fig. 5). The observed two peaks (no. 12834) may be the same as the ones predicted.

C. History of the experimentally observed HWHM of the core emission

As explained in Sec. IV A, we can assume from the simulation that the HWHM of the spatial profiles of the x-ray core emission represents the location of the contact surface. For the liquid-fuel cryogenic targets considered here, the observed x-ray emission happens to follow the simulated shock trajectory in the saturated D_2 vapor before the collapse at the center (Figs. 3–5). This indicates that the contact surface follows the same hydrodynamic motion as the one initially predicted for the shock. The real shock in the experiment should propagate faster,

consistent with our observation of the emission at the center [Fig. 7(a)], which could be due to the shock collapse. This central emission is followed by the two-peak emission due to the reversed shock colliding with this interface. If a minor shell breakup occurred in the shell due to Rayleigh-Taylor instability, as modeled by Katayama [18] for experiments using similar foam targets, then these shock propagations and the following preemission could be explained. It is important to note that the shell breakup should be minor if there is any. As shown in Fig. 1, the overall implosion is achieved rather spherically and the main shell stayed cold surrounding the hot

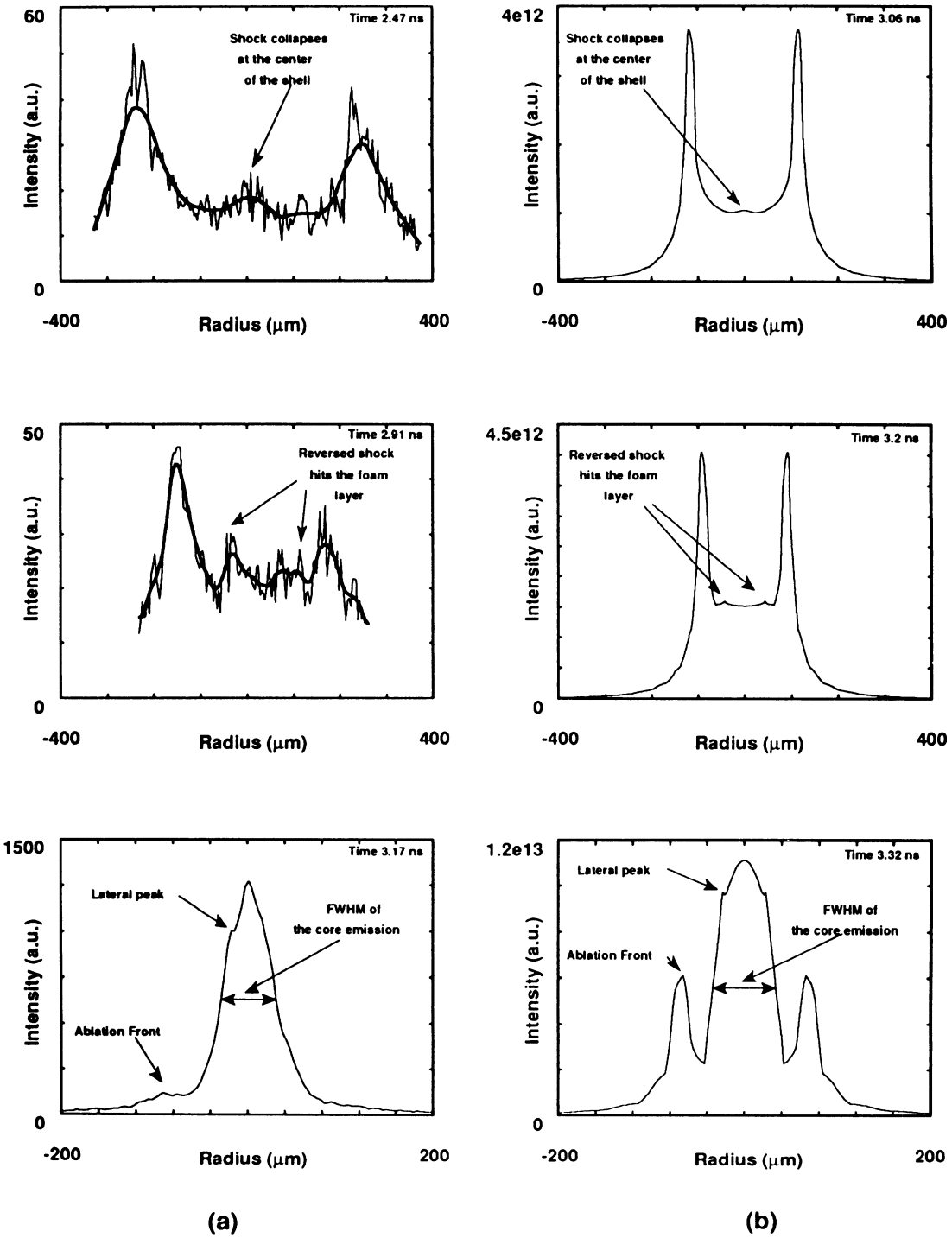

FIG. 7. Radial profiles of the XSC recorded emission for shot no. 12865, at different timing. (a) Experiment. Bold line shows an average fit on the data. (b) Simulation. The central emission due to the shock collision and small double peaks due to the reversed shock colliding with the imploding shell appear common between the experiment and simulation. In the simulation the HWHM of the core emission represents the radial boundary between the hot core and the cold fuel layer.

core at the stagnation. Some of the fragments from the shell breakup could fly much faster than the average shell implosion speed.

The contact surface is stopped, probably by the pressure of the fuel and the residual vapor. The maximum of the x-ray emission takes place at the end of the maximum compression phase at the contact surface just before it expands. The contact surface maximum compression radii are 24, 25, and 28 μm in the experiment, very close to the shell density interface maximum compression radii predicted by the 1D HISHO code, 18, 27, and 28 μm. From these values we can derive an experimental convergence ratio at the contact surface: 12.4, 10.6, and 12.5. These values can be compared to the values predicted by the code: 33, 12, and 17.5. Shot no. 12834, showing a relatively large difference compared to the simulated value, is the one for which the prediction was the best. On shot 12847 the observed convergence ratio reaches 88% of the simulated one. This shot was performed under the lowest beam energy imbalance, consistent with the good convergence.

V. CONCLUSION

We summarize our study as follows. The ablation front trajectories derived from XSC data agree well with the 1D HISHO simulation in the acceleration and inertial phases. The compression appears halted earlier than predicted. We observe a preemission, which is the x-ray emission of the core recorded by the XSC starting earlier and having a duration longer than the simulated one. The experimental time profiles of the core x-ray emissions show qualitative agreement with the simulations. We make the following observations. (1) The timing of the shock propagation can be observed. (2) Around the maximum compression, the ablation front location given by the XSC is not representative of the shell surface. (3) The HWHM of the core emission gives the location of the contact surface with a good precision (~ 5 μm) for the liquid- and solid-fuel shells. The experimental HWHM of the x-ray core emission trajectory reaches a minimum radius of the same order as the simulated shell density interface. The convergence ratios at the contact surface, calculated from this HWHM, are 0.4, 0.9, and 0.7 times those predicted, respectively, for the liquid-fuel shots 12834, 12847, and 12865. The best convergence was obtained for the least beam energy imbalance.

ACKNOWLEDGMENTS

We are grateful to the members of the laser, experimental, and target groups and particularly to M. Saitoh, M. Takagi, and O. Maekawa, without whom that experiment would not have been possible. One of the authors (A.R.) has been supported under Contract DRET No. 911463/A000/DRET/DS/SR.

[1] F. J. Marshall, S. A. Letzring, C. P. Verdon, S. Skupsky, R. L. Keck, J. P. Knauer, R. L. Kremens, D. K. Bradley, T. Kessler, J. Delettrez, H. Kim, J. M. Soures, and R. L. McCrory, Phys. Rev. A **40**, 2547 (1989).

[2] H. Azechi, T. Jitsuno, T. Kanabe, M. Katayama, K. Mima, N. Miyanaga, M. Nakai, S. Nakai, H. Nakaishi, M. Nakatsuka, A. Nishiguchi, P. A. Norrays, Y. Setsuhara, M. Takagi, M. Yamanaka, and C. Yamanaka, Laser Part. Beams **9**, 193 (1991).

[3] M. Nakatsuka, T. Jitsuno, T. Kanabe, S. Urushihara, N. Miyanaga, and S. Nakai, in *Pulse Power for Lasers III,* edited by G. G. McDuff, SPIE Proc. Vol. 1411 (SPIE, Bellingham, WA, 1991), p. 108.

[4] Y. Kato, K. Mima, N. Miyanaga, S. Arinaga, Y. Kitagawa, M. Nakatsuka, and C. Yamanaka, Phys. Rev. Lett. **53**, 1057 (1984).

[5] T. Yamanaka *et al., Plasma Physics and Controlled Nuclear Fusion Research 1992, Proceedings of the 14th International Conference on Plasma Physics and Controlled Nuclear Fusion Research,* Warzburg, Germany (International Atomic Energy Agency, Vienna, 1993).

[6] M. Takagi, T. Norimatsu, T. Yamanaka, and S. Nakai, J. Vac. Sci. Technol. A **9**, 820 (1991).

[7] M. Takagi, M. Ishihara, T. Yamanaka, and S. Nakai., Jpn. J. Polym. Sci. Technol. **49**, 661 (1991) (in Japanese).

[8] T. Norimatsu, H. Ito, C. Chen, M. Yasumoto, M. Tsukamoto, K. A. Tanaka, T. Yamanaka, and S. Nakai, Rev. Sci. Instrum. **63**, 3378 (1992).

[9] B. L. Henke, J. P. Knauer, and K. Premaratne, J. Appl. Phys. **52**, 3 (1981).

[10] M. Katayama, M. Nakai, T. Yamanaka, Y. Izawa, and S. Nakai, Rev. Sci. Instrum. **62**, 124 (1991).

[11] H. Azechi, N. Miyanaga, R. O. Stapf, K. Itoga, H. Nakaishi, M. Yamanaka, H. Shiraga, R. Tsuji, S. Ido, K. Nishihara, Y. Izawa, T. Yamanaka, and C. Yamanaka, Appl. Phys. Lett. **49**, 555 (1986).

[12] S. Nakai, Laser Part. Beams **7**, 467 (1989); C. Yamanaka, *Handbook of Plasma Physics* (North-Holland, Amsterdam, 1991), Vol. 3, p. 1.

[13] K. A. Tanaka, Institute of Laser Engineering Quarterly Progress Report, Osaka Univ. Jan. 1988–March 1988 No. 25, 1989 (unpublished).

[14] S. Nakai *et al.*, in *Laser Interaction and Related Plasma Phenomena,* edited by H. Hora and G. H. Miley (Plenum, New York, 1991), Vol. 9.

[15] P. A. Jaanimagi, J. Delettrez, G. G. Gregory, R. S. Marjoribanks, and M. C. Richardson, in *High Speed Photography, Videography and Photonics V,* edited by H. C. Johnson, Proc. SPIE Vol. 832 (SPIE, Bellingham, WA, 1987), p. 368.

[16] M. Murakami and K. Nishihara, Jpn. J. Appl. Phys. **26**, 1132 (1987).

[17] K. A. Tanaka, T. Yamanaka, K. Nishihara, T. Norimatsu, M. Nakai, R. Kodama, M. Nakatsuka, T. Kanabe, T. Jitsuno, H. Azechi, K. Mima, N. Miyanaga, A. Nishiguchi, H. Takabe, C. Chen, M. Kado, M. Katayama, M. Tsukamoto, and S. Nakai, in 21st European Conference on Laser Interaction with Matter, Warsaw, 1991, edited by H. Fiedorowicz and J. Wolowski (to be published).

[18] M. Katayama, Ph.D. thesis, Osaka University, 1993 (in Japanese) (unpublished).

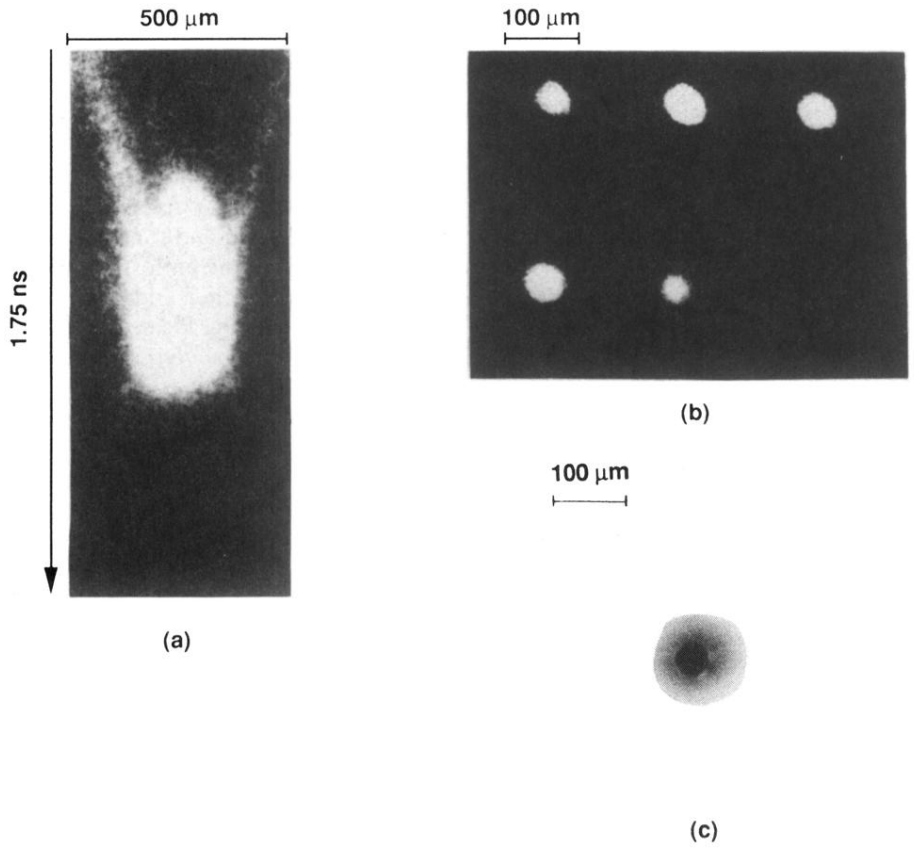

FIG. 1. Records of the x-ray emission for the liquid-fuel shot no. 12865. (a) The XSC imaging system. (b) The second XFC imaging system, around maximum compression. (c) The pinhole imaging system.